Rifting through a stack of inhomogeneous thrusts (the dipping pie concept)

Laetitia Le Pourhiet, Evgenii E.B. Burov, Isabelle Moretti

Rifting through a stack of inhomogeneous thrusts (the dipping pie concept)

Laetitia Le Pourhiet[1]

Institut Français du Pétrole, Rueil Malmaison, France

Evgenii Burov

Laboratoire de Tectonique, UMR 7072, Université Pierre et Marie Curie, Paris, France

Isabelle Moretti

Institut Français du Pétrole, Rueil Malmaison, France

[1] Orogenic building leaves a complex heritage consisting of a stack of nappes that may have contrasting lithologic structures resulting in heterogeneous mechanical behavior of the system during the postorogenic stages. While the thermal state of the region is reequilibrating, strong lateral variations of the depth to the brittle-ductile transition develop as a consequence of these preexisting heterogeneities. We use a thermomechanical model to quantify how an inherited weak nappe influences the development of fault patterns resulting from postorogenic extension. The competence contrast between the nappe and the rest of the upper crust as well as the strength of the crust itself are the principal variable parameters of our experiments. The results suggest that a dipping weak nappe introduces a lateral velocity discontinuity and serves as a localization factor for deformation. The presence of a preexisting nappe with a low competence contrast is sufficient to localize strain along the nappe leading to the formation of a flexural rolling hinge. In this case, the migration of the basin is slow, continuous, and limited by gravity driven processes that lead to the rise of hot (weak) material under the subsiding basin. In case of a high competence contrast, overall crustal strength is reduced by a "dipping pie" effect. Assuming overall high crustal strength, the presence of a contrasting nappe leads to a bimodal fault pattern governed by two types of faults: crustal-scale planar faults rooting on the brittle ductile transition of the crust and thin-skinned listric faults rooting on the nappe itself. This bimodality results in a jump-like migration of the basin downward along the dipping weak nappe. Applying this model to the case of the Gulf of Corinth (Greece) allows us to explain, in the case of assumed high competence contrast, the observed microseismicity patterns, the asymmetry of the Gulf, and the kinematics of fault migration within the basin. *INDEX TERMS:* 3210 Mathematical Geophysics: Modeling; 8015 Structural Geology: Local crustal structure; 8105 Tectonophysics: Continental margins and sedimentary basins (1212); 8109 Tectonophysics: Continental tectonics—extensional (0905); *KEYWORDS:* rifting, Corinth, numerical modeling, tectonic heritage. **Citation:** Le Pourhiet, L., E. Burov, and I. Moretti (2004), Rifting through a stack of inhomogeneous thrusts (the dipping pie concept), *Tectonics*, *23*, TC4005, doi:10.1029/2003TC001584.

1. Introduction

[2] In various regions of continental deformation, the orogenic phases are followed by postorogenic extension. In these zones, geological and geophysical field observations reveal preexisting upper crustal structures such as relics of foreland basins with preserved characteristic napping structures. Analysis of these structures suggests the presence of large rheological inclusions with highly contrasting properties that may induce strong lateral variations in the depth of the brittle-ductile transition if a weak nappe with an inherited dip finds itself in a zone of active deformation. This study focuses on the influence of rheological contrasts found in the ancient thrust sheets on the overall evolution of a rift system during extension. Particular attention is paid to the control exerted by such inherited heterogeneity on the normal fault pattern and kinematics. A very simple initial geometry composed of a single weak nappe with a flat and ramp geometry is used to simulate an inherited foreland. The main parameters of the numerical study are the competence contrast between a weak dipping nappe and its surrounding rock, and the competence of the surrounding rock itself. For each case, the distributions of brittle deformation and the resulting geometry of brittle-ductile transition are computed and put in a phase diagram.
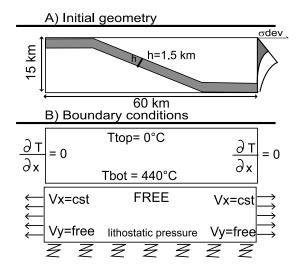
[3] The regional part of the study attempts to explain the recent observations made in the western part of the Gulf of

---

[1]Now at Laboratoire de Tectonique, Université Pierre et Marie Curie, Paris, France.

Figure 1. Initial and boundary conditions. (a) Initial geometry corresponds to a common flat and ramp structure with a weaker nappe in gray which thickness is 1.5 km. The choice of the initial geotherm is not crucial since we test a wide range of rheological parameters to cover the effects of possible uncertainties in the temperature profile. (b) Boundary conditions correspond to symmetric stretching with free vertical slip on the left and right borders, Winkler basement at depth and true free surface boundary condition is applied at the top. The temperatures are kept constant at the top and at the bottom (0°C and 440°C, respectively), while the lateral boundary conditions correspond to zero lateral outflows.

Corinth by taking into account the complexity of the prerift basement. Field studies as well as geophysical data have shown that the Phyllades nappe is the main lithological contrast in the prerift basement of the Gulf of Corinth, its thickness and its dip are known but the rheological properties of the rocks of the prerift basement are very poorly constrained. The numerical models are used to understand if the Phyllades nappe can explain the dynamic and local kinematics of the Gulf.

2. Modeling Approach

2.1. Initial Model Geometry and Assumptions

[4]   We have constructed our model in a way that allows us not only to study the particular case of the Gulf of Corinth but also to encompass more general settings. For this reason, we have neglected some specific details of secondary importance and retained those common to many postorogenic systems:

[5]   The model box (Figure 1a) is 60 km long and 15 km deep. A nonplanar heterogeneity corresponding to the nappe is introduced in the box. This heterogeneity presents a 1.5 km wide band characterized by a weak material phase. The introduced "nappe" flattens at the horizontal borders of the model to reproduce the usual flat and ramp geometry of real nappes. Mechanically speaking, the upper flat portion

of the nappe does not affect the predicted deformation patterns because the near-surface deformation is dominated by elastoplastic behavior, whereas the imposed elastoplastic properties are the same both for the heterogeneity and for the host rock. The presence of a flat weak segment at the bottom of the model does not really reduce the integrated strength of the upper crust because the strength of the host rocks is already low at depth.

2.2. Method

[6]   We use thermomechanically coupled code PARA (O)VOZ [*Poliakov et al.*, 1993]. Its algorithm is based on Fast Lagrangian Analysis of Continuum (FLAC® [*Cundall*, 1989]). PARA(O)VOZ is a hybrid finite element/difference, fully explicit time-marching Lagrangian algorithm operating in large strain mode. This code directly solves Newton's equations of motion instead of more commonly used static stress balance equations. In addition, the Lagrangian scheme allows us to replace the solution of Newton's full equations of motion in large strain mode by a dynamically updated solution of these equations in small strain mode:

$$\rho g_i + \frac{\partial \sigma_{ij}}{\partial x_j} = \rho \frac{\partial V_i}{\partial t}, \tag{1}$$

[7]   Equation (1) is coupled with constitutive laws corresponding either to a non-Newtonian viscoelastic Maxwell body (if the yield criterion for Mohr Coulomb plasticity ($f = 0$) is not reached), or to an elastoplastic Mohr-Coulomb body if f reaches zero. Details about the numerical implementation of the rheology and related stress update procedures are provided in Appendix A. Equation (1) is coupled with the heat transfer equation

$$\frac{DT}{Dt} = \frac{\partial}{\partial x_i}\left(\chi\frac{\partial T}{\partial x_i}\right) + \frac{H_r}{\rho C_p}, \tag{2}$$

in which the advective part of DT/Dt is solved together with equation (1) and T (temperature) is used for computation of temperature-dependent viscosity and thermal stresses. The parameters ρ, σ, x, V, t, T, χ, C_p, and Hr stand for density, stress, coordinate, velocity, time, temperature, thermal diffusivity, specific heat and internal heat generation, respectively. D/Dt means objective time derivative.

[8]   The algorithm was already tested on many extensional problems [e.g., *Poliakov and Buck*, 1996; *Burov and Poliakov*, 2001]. The description and benchmarks of the algorithm can be found in FLAC-related literature [e.g., *Cundall*, 1989; *Poliakov et al.*, 1993]. The main advantage of this relatively slow method relates to its ability to treat practically any rheologies (strongly nonlinear, hardening, softening, etc). In particular, the algorithm allows the faults (shear bands) to form during loading in a self-consistent way. As in nature, the location of the brittle-ductile transition is not predefined a priori, but is reevaluated on each time step as a function of local strain rate, stress, and temperature. Thus it is possible to make direct comparisons between the predicted depth and geometry of the brittle

Table 1. Lithological Phases Rheological Parameters

Phase	Density, ρ, kg m^{-3}	A, MPa^{-n}	N	E, J mol^{-1}	Young's Modulus, E, Pa	Cohesion, Pa, C_0	Friction Angle, ϕ, deg
1	2600	5×10^3	3	1.9×10^5	7.5×10^{10}	2×10^7	30°
2	2600	5×10^0	3	1.9×10^5	7.5×10^{10}	2×10^7	30°
3	2600	5×10^{-3}	3	1.9×10^5	7.5×10^{10}	2×10^7	30°
4	2600	5×10^{-6}	3	1.9×10^5	7.5×10^{10}	2×10^7	30°

ductile transition and the observed thickness and geometry of the seismogenic crust.

3. Model Setup

[9] The initial and boundary conditions are schematically represented in Figure 1. The experiments were restricted to upper crustal scale, which permits us to model fault migration with high numerical resolution (200 m per grid element). This precision allows us to consider as geologically relevant predicted fault spacing greater than 1 km.

3.1. Boundary Conditions

[10] A true free surface boundary condition is applied at the upper surface of the model. This boundary condition is combined with slow surface erosion, which is implemented using a common diffusion law [e.g., *Culling*, 1960]:

$$\frac{\partial h}{\partial t} = Ks\nabla^2 h, \qquad (3)$$

where h is topography elevation, t is time, and Ks is the coefficient of erosion. At the bottom we impose the Winkler boundary condition, which represents a combination of a free horizontal slip with vertical forces equivalent to isostatic reaction of a viscous substratum of a constant density (2600 kg m^{-3}). At the horizontal borders, constant horizontal velocities (one of the variable parameters of the experiments) are applied in combination with a vertical free slip boundary condition. The thermal boundary conditions are imposed by maintaining fixed temperatures at the horizontal borders of the model and by a null outflow boundary condition at the vertical borders. The initial thermal distribution is computed using the commonly inferred nonstationary half-space cooling model of the lithosphere [*Parsons and Sclater*, 1977] with the same boundary conditions and assuming a thermotectonic age of 150 Myr.

3.2. Model Parameters

[11] The principal variable parameters of the experiments are (1) the extension rate, (2) the dip of the weak nappe, and (3) the competence contrast between the nappe and the surrounding rocks. The initial geotherm was kept unvaried. Instead, to vary the depth of the brittle ductile transition, we varied the preexponential term of the dislocation creep law in the range compatible with the range of experimental parameters of the ductile creep flow law for quartz-dominated rocks [*Brace and Kohlstedt*, 1980; *Hansen and*

Carter, 1982; *Kirby and Kronenberg*, 1987; *Ranalli*, 1987; *Tsenn and Carter*, 1987]. The modeled phase rheological parameters are summarized in Table 1.

3.3. Description of the Experiments

[12] We have conducted a series of experiments to study the influence of a dipping nappe on fault patterns and kinematics. The preliminary tests were focused on the influence of its dip assuming a fixed competence contrast between the nappe and its surrounding rock (phases 2 and 4). The value of the dip angle was varied between 0° and 30°. The trivial case with zero dip (0°) does not produce any valuable results since the strain localizes at the borders of the model as long as there is no important velocity contrasts inside the model area. The experiments with a dip angle of 20° appear to be the most interesting as they demonstrate the most significant differences in the mechanical behavior of different phases.

[13] The aim of the other set of numerical experiments was to understand how the presence of a weak dipping heterogeneity in the prerift basement influences the faulting patterns and the kinematics of the deformation in the crust. These experiments are grouped in three subsets that correspond to three main varying parameters: (1) competence contrast (i.e., associated with brittle-ductile transition depth) between the host rock and the dipping heterogeneity (models 1a, 2a, 3a); (2) strength of the host rock (models 2a, 2b, and 3a, 3b, 3c); (3) background strain rate (models 1a, 1b, 1c).

[14] Table 2 summarizes the physical parameters (i.e., phases used for the matrix and the heterogeneity, applied background strain rate) used for each of the experiments.

4. Results

[15] In the following description of the experimental results, we will call "synthetic" the faults that form with the same downdip direction as the nappe. Those that form in the opposite direction will be called "antithetic." "Basin migration" means here the relative displacement of its depocenter and may be either continuous in time (small displacements at a constant rate), or discontinuous in time when the depocenter "jumps" covering several kilometers in one leap.

4.1. Influence of the Competence Contrast

[16] For low competence contrasts (Figure 2c), flexural slip on the nappe is the dominating mode of deformation. The entire normal faults root on the nappe. The slow and

Table 2. Physical Parameters Used for Each Experiment

Model	Host Rock Phases	Nappe Phases	Divergent Velocity, cm yr^{-1}	Background Strain Rate, s^{-1}
1a	4	1	1	5×10^{15}
1b	4	1	1.5	1×10^{-14}
1c	4	1	0.5	2.5×10^{-15}
2a	4	2	1	5×10^{-15}
2b	3	1	1	5×10^{-15}
3a	4	3	1	5×10^{-15}
3b	3	2	1	5×10^{-5}
3c	2	1	1	5×10^{-15}

continuous migration of the basin provokes very localized isostatic rebound and consequently upward flow of weak material phases toward the surface. The kinematics corresponds to a common flexural rolling hinge model [*Axen*, 1992; *Axen and Bartley*, 1997; *Kaufman and Royden*, 1994] (Figure 3, case C).The second invariant of deviatoric stress tensor indicates that elastic flexural bending around the inherited nappe is very important (Figure 2c, 20–30% of stretching) and leads to flexural uplift of the footwall of the graben.

[17] For very high competence contrasts (Figure 2a) the number of active normal faults increases with time. The flexure is completely accommodated by faulting both above and below the weak nappe decreasing the effect of footwall uplift. The major planar faults root on the brittle-ductile transition (BDT) of the host rock and form an upper crustal-scale system of horsts and grabens while some minor faults continue to root on the nappe. The migration of the basin is controlled by the migration of the major planar faults, i.e.,

by the strength of the surrounding crust. When a new planar fault appears downward along the nappe, the older basins (left side of our model) uplift as a result of local isostatic compensation. This uplift is accommodated by an antithetic fault (type I, Figure 3, case D) formed out-of-sequence. At the same time, minor out-of-sequence faults (type II, Figure 3, case D) develop at the top of the horst because the horst includes a part of the nappe, which is rigidly translated upward.

[18] For intermediate competence contrast (Figure 2b), both faulting and flexural slip occur to accommodate flexural deformation. In the early phase, high competence contrast mode is preferred, because the deformation occurs in the shallow part of the model. In the later stages, the deformation localizes deeper and low competence mode prevails, the number of faults decreases and strain tends to localize on the last synthetic fault.

[19] Finally, the competence contrast also controls the shape of the final topography of the rift (Figure 4a). For low and medium competence contrast, as flexural bending is favored at the end, the final topography is rounded, while for low competence contrast, faulting accommodation of flexure flattens it, leaving accidents located near the major faults.

4.2. Second-Order Controlling Parameters

4.2.1. Strength of the Host Rock

[20] For constant strain rate and constant competence contrast, the strength of the surrounding material controls the quantity of flexural deformation to be accommodated elastically or plastically (brittle). In both cases, this includes controls on the maximum height of the topography (Figure 4b). Less intuitively, it also controls the timing of

Figure 2. Second invariant of stress and cumulative plastic strain. For all models presented here, the viscoelastoplastic rheological parameters of the host rocks (phase 4, Table 1) and of the background strain rates are identical, only the competence contrasts vary. Effective shear stress is shown here for high, intermediate, and low competence contrasts at different stages of stretching (5, 10, 20, and 30%). The purple color corresponds to the highest deviatoric stress. The bottom pictures in each column represent cumulated plastic (brittle) strain. The blue regions are those which always deform viscously. The red color represents zones where accumulated brittle strain is very high (these parts are interpreted as major faults). At each step, the currently active faults, on which the current strain rates are highest, are marked with dashed lines. At 5% stretching, all models have their integrated strength (deviatoric stress integrated on a vertical profile in the faulted zone) reduced at the level where faulting takes place. The model with the highest integrated strength is the model with low competence contrast. The model with very high competence contrast has almost negligible strength. (a) High competence contrast (model 1a). Between 10 and 20% stretching, basin migrates, strain is distributed, because (1) the nappe is so weak that it is always easier to break somewhere else and (2) the decollement level is very shallow and many faults are needed to accommodate strain. At 30% stretching, many synthetic faults are active, the subsiding basin is 13 km wide, and the stress patterns do not indicate any localized weakening of the crust. Plastic strain indicates that four major faults were formed during the deformation. (b) Intermediate competence contrast (model 2a). In this case, the basin does not migrate as much as in the case of the high competence contrast, but the number of the active faults increases with time as the width of the basin increases. The nappe behaves as a level of decollement where the faults are refracted, which causes faulting to be shifted between surface and depth. At 30% stretching, the crust is weakened locally by an upward flow of hot lower crust induced by an isostatic response to surface unloading. The thinning of the crust is symmetric even if synthetic faults are predominant. Plastic strain indicates that two major faults were formed during the deformation. (c) Low competence contrast (model 3a). From 5 to 30% stretching, the width of the subsiding basin decreases from 30 km to 15 km. The depocenter migrates smoothly in the dipping direction of the nappe by a rolling hinge mechanism until 20% stretching. At that point, the crust is weakened locally by hot lower crust material. The migration is fast because none of the faults accumulate important strain, apart from the last one where strain finally localizes. See color version of this figure at back of this issue.
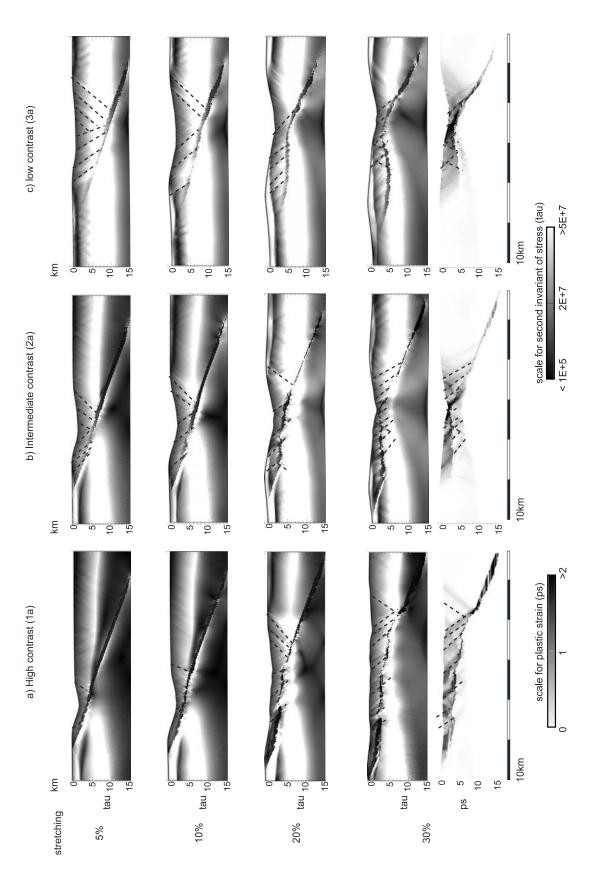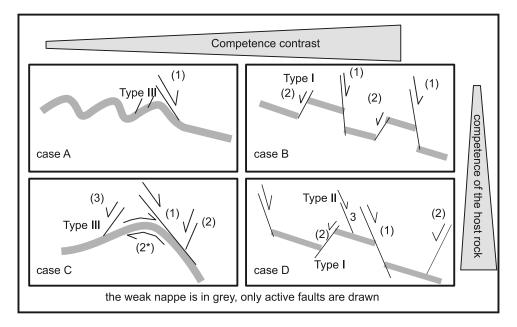
Figure 2

Figure 3. Phase diagram for faulting pattern. Presented are four cases of the computed fault patterns predicted as a function of the competence contrast ($A_{host\ rock}/A_{nappe}$) and of the competence of the host rock ($\alpha A_{host\ rock}$). For thin nappes, the competence of the host rock constrains the wavelength of the deformation, while the competence contrast constrains the type of accommodation of flexure beyond the major normal fault (1). For low competence contrast, flexure is accommodated on the nappe by flexural slip (2*). For high competence contrast, flexure is accommodated on antithetic faults (2). The three types of out-of-sequence faults are described. Type III corresponds to a very late stage of deformation and develops only when the downdip direction of the nappe switches from north to south at the back of the major faults. Type I and II are characteristic of the high competence contrast mode. Type I corresponds to the antithetic faults described by *Axen and Bartley* [1997] for the basins and ranges; they help to accommodate flexure and uplift. The antithetic faults of type II are characteristic of the high competence contrast mode with high competence of the host rock; they develop to accommodate stretching in the upper block during its uplift.

the beginning of the uplift of the older basin that happened at 20% of stretching in the case of high competence host rock (phase 4), 15% of stretching in the case of medium competence host rock (phase 3) and only 10% of stretching in the case of low competence host rock (phase 2). Dynamically, the beginning of the uplift is associated with the formation of out-of-sequence antithetic faults of type I (Figure 3, cases D and B) and Type III (Figure 3, other case). The lowest is the strength of the host rock, the shortest are the wavelengths implied in the uplift of the older basin and the fastest the antithetic faults are developing.

4.2.2. Background Strain Rate

[21] As shown in section 4.2.1, the uplift begins when the first antithetic fault develops. In models 1a, 1b and 1c, the antithetic faulting (Figure 3, Type I) inception has different timing. It happens after 10% of stretching for a high background strain rate (Figure 5b), 15% of stretching for a medium background strain rate (Figure 5a), and 20% of stretching for a low background strain rate (Figure 5c). Strain rate also controls the timing of the uplift. Considering the host rock behaves as a viscoelastic body, its integrated strength depends on strain rate. The antithetic faulting timing is now clearly related to the relative quantity of

viscous relaxation versus Mohr-Coulomb plastic relaxation of stress. The highest is the background strain rate and the longest is the viscous stress relaxation time, favoring the occurrence of Mohr-Coulomb plasticity.
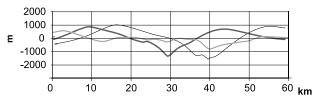
5. Interpretation

[22] The presence of a weak dipping nappe causes a reduction in the overall strength of the crust for the same reason that a multilayered media (alternation of weak and strong layer) is weaker than a single strong layer of a thickness equivalent to the sum of the strong layer thickness. Our model thus presents a kind of dipping pie. The comparison with previous horizontally homogeneous models has to be made carefully because, contrary to most of the previous rifting models, our setup is not at lithosphere scale. The "elastic" or "rigid" layer we consider is the upper crust.
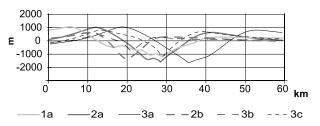
5.1. What Does the Dipping Pie Change in Terms of Fault Spacing?

[23] Two main approaches exist to study fault spacing: the flexural models and the horizontally layered models

A) Topography after 30% stretching

B) Maximum topography during experiments

——— 1a   ——— 2a   ——— 3a   — — 2b   — — 3b   - - - 3c

Figure 4. Topography. (a) After 30% stretching, topography of low and medium competence contrast models is rounded by flexural bending, while the high competence contrast model topography reflects a lack of flexural elastic bending with local roughness located at the major normal faults. (b) Maximum topography reached during calculation: models with the same competence of the host rock reach similar maximum topography. Maximum topography decreases with the competence of the host rock.

(basically one dimensional). One-dimensional large-scale rift models [e.g., *Buck*, 1991] are based on the evaluation of forces needed to extend the lithosphere at a constant rate while localization is imposed. If stretching leads to local weakening, the basin does not migrate (narrow rift mode), whereas, if stretching leads to local hardening, the basin migrates further (wide rift mode). Two major differences thus exist between these and our models: (1) One-dimensional models by *Buck* [1991] predefine localization and assume pure shear. (2) These models have infinite lateral dimensions, whereas our models are small scale, which limits their predictions for wide rift mode. Nevertheless, our models still respect the basic rules suggested by *Buck*'s [1991], although in a nontrivial way: (1) in the case of overall high strength of the crust (i.e., low competence contrast), our models predict "narrow rift mode" at the onset of the rise of the ductile material, which is equivalent to a one-dimensional weakening of the crust and thus to *Buck*'s [1991] narrow rift mode. (2) In the case of low overall crustal strength (high competence contrast), the crustal-scale faults also annihilate the local one-dimensional weakening in our model. However, their spacing cannot be really compared to the "wide rift" mode described by *Buck* [1991]. Yet, such planar faults can be explained by alternative thin plate models. Pure flexural models [e.g., *Heiskanen and Meinesz*, 1958] predict that new faults form in zones of maximal shear stress. For a constant strength elastic layer resting on viscous semi-infinite space, the fault spacing is controlled

by the thickness of the elastic layer [e.g., *Spadini and Podladchikov*, 1996]. The bottom of our model can indeed be considered as an infinite inviscid layer (Winkler boundary condition), but the estimated equivalent elastic thickness EET [e.g., *Burov and Diament*, 1995] plotted both for high and low competence contrast in Figure 6 shows that the nappe strongly affects the integrated strength profile and that no obvious simple solution can be found in this case. Nevertheless, in the case of high competence contrast, the EET is reduced by half, which explains the spacing of planar faults. These faults cannot be formed for low competence contrast because of the horizontal size of the model.
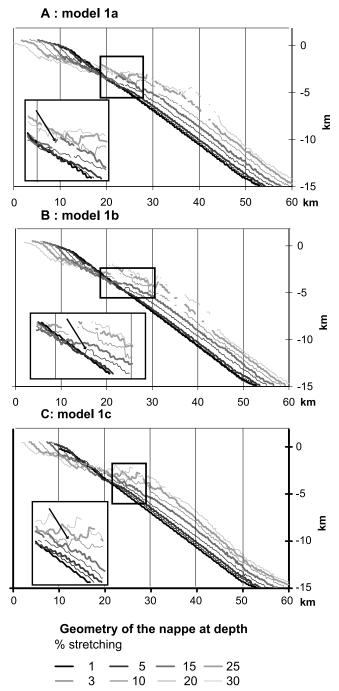
5.2. Dipping Pie and Detachments/Rolling Hinge Concept

[24] *Axen and Bartley* [1997] recognized in the Basins and Ranges province two major modes of accommodation of flexural deformation: flexural slip and antithetic faulting. In our study, both modes coexist and their relative importance depends primarily on the competence contrast between the nappe and its host rock (Figure 3). These different modes of flexural accommodation result in important differences in terms of produced fault patterns.

[25] Detachment models [e.g., *Melosh*, 1990] are comparable to our model in terms of initial geometry. This author considers that in the case of a preexisting mylonite zone, the fault spacing is conditioned by the ability of the weak mylonitic heterogeneity to accommodate strain. Major differences between both problems are that the depth and the viscosity of the mylonitic zone are predefined and kept constant in *Melosh*'s [1990] setup. In our model, the effective viscosity is dynamically recomputed as a function of local stress, strain rate, and temperature. As a result, it varies within orders of magnitude. As a consequence, the locations of new major faults depend not only on the strength of the nappe itself but also on the competence contrast between the nappe and the host rock (otherwise, if this was not the case, the fault patterns would be identical in experiments 2b and 1a).

5.3. Dipping Pie and Out-of-Sequence Faulting

[26] Out-of-sequence faulting occurs in the experiments that include a weak dipping nappe (e.g., the fault that appears in the footwall of the active faults at a given time). For high competence contrasts, two types of out-of-sequence faults can be distinguished: Type I faults, which are defined as those (Figure 3) that dip in the opposite direction from the initial dipping direction of the nappe, and Type II, which are defined as those which dip in the same direction as the initial dipping direction of the nappe. The faults of Type I accommodate the uplift of the footwall and relate to the same mechanism as those described by *Bertotti and Podladchikov* [2000]. The faults of Type II can be explained by a different model, which relates fault spacing to the depth of the decollement zone [e.g., *Spadini and Podladchikov*, 1996; *Montési and*

A : model 1a

B : model 1b

C: model 1c

Geometry of the nappe at depth
% stretching

— 1	— 5	— 15 — 25
— 3	— 10	— 20 — 30

Figure 5. Timing of the localization of the first antithetic fault in the case of high competence contrast. The curves plotted here correspond to the geometry of the nappe at depth. In the case of high competence contrast, it is possible to point out when the first antithetic fault happened because the nappe is suddenly shifted. A higher value of mean strain rate implies that faulting happened earlier (10% for model 1b, 15% for model 1a, and 20% for model 1c).
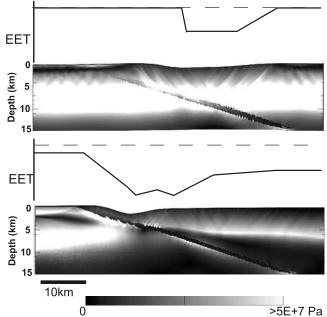
Zuber, 2003]. These faults form only in the high competence contrast mode because only in this case is the nappe included in the horst uplifted by the faults that root at the BDT of the host rock. Once the decollement

level reaches shallower depths, new faults must form to accommodate extension in the upper block.
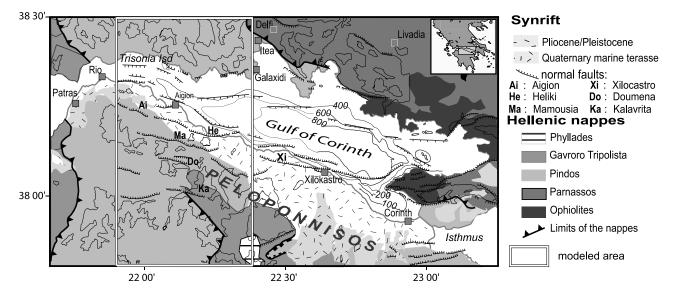
6. Conclusion and Discussion (Numerical Part)

[27] Although the thickness of the Phyllades nappe was introduced in the model as input data and not as a variable parameter, it is clear that the presence of a weak nappe is equivalent to mechanical decoupling in the upper crust.

[28] The resulting strength of this discontinuous crust decreases as the third power of the thickness of the weak layer. Thus variation in the thickness of the layer by 1 order of magnitude is equivalent to variation in its strength (viscosity) by 3 orders of magnitude. In our situation, we can consider that increasing the thickness of the weak layer is mechanically equivalent to an increase in the competence contrast ($A_{\text{nappe}}/A_{\text{host rock}}$) at a fixed thickness of the weak layer. In other words, if the 1.5 km thickness used for the study overestimates the actual thickness of Phyllades nappe, the competence contrast needed to fit the data must be higher than the one that we have found. As this competence contrast is already very large, other weakening factors must be

Figure 6. Equivalent elastic thickness (EET) profiles. The EET profiles show that in both cases the synthetic faults root at depth where the EET attains a lateral minimum. In the low competence contrast case, the nappe does not mechanically decouple the upper crust, and thus the EET profile is not affected. By comparison, in the case of a high competence contrast, the crust is mechanically decoupled and EET is much lower then in the first case. Note that in this case, the EET profile has two minima, and that the second corresponds to the place where the next fault is going to develop.

Figure 7. Geological map of the Gulf of Corinth. The extensional lineations (striped on the map) trend N30°–50° in the metamorphic window of Pheneos (L. Jolivet, personal communication, 2002). Hellenic nappes after *Jacobshagen et al.* [1978]; recent faults after *Rigo et al.* [1996], *Ghisetti et al.* [2001], and *Moretti et al.* [2003].

added to the model. On the other hand, for larger thickness, the high competences contrast mode of deformation will be reached for much smaller viscosity contrast than it was in this study.

[29] A number of other important conclusions may be drawn on the basis of the experiments of this study. In particular, our results suggest that the presence of a weak dipping crustal heterogeneity such as an ancient nappe strongly influences the style of deformation during post-orogenic rifting and may result in a complete asymmetry of the produced faulting, subsidence and uplift patterns. The competence contrast between the heterogeneity and the background rock is a major controlling factor on the mode of rifting, which can vary from the "narrow" rift mode, in the case of a low competence contrast, to the "wide" rift mode in the case of high competence contrast. When the narrow rift forms, the uplift of the rift shoulders is important and is controlled by flexure, while in the case of a wide rift, the uplift is less prominent and is controlled by local isostatic balance. In both cases, the uplift is strongly asymmetric even when the boundary conditions are symmetric.

7. Application to the Western and Central Gulf of Corinth

[30] The Gulf of Corinth is an active rift zone associated with very high seismicity and strain rates. It is located between Peloponnesus and continental Greece. All recent studies confirm that the rifting was initiated 1 Myr ± 0.2 ago [*Sorel*, 2000; *Westaway*, 2002; *Moretti et al.*, 2003]. The recent GPS data [*Briole et al.*, 2000] infer an opening direction N00 with opening velocity decreasing eastward from 1.5 cm yr^{-1}, at Rio, to 0.5 cm yr^{-1}, at the level of the Isthmus of Corinth.

[31] The main inherited features in the region of Corinth are some preexisting variations in crustal thickness (discussed by *Le Pourhiet et al.* [2003]) and the Phyllades nappe outcrops south of the Gulf. Both are related to the orogenic building and to the Miocene times extension. The Phyllades nappe is mainly composed of weak phyllosicates (L. Jolivet, personal communication, 2002) (see map in Figure 7) and shows lineation of extension N30 to N50. We proposed to apply our model to the Phyllades nappe which is the major lithological contrast in the area. Considering this, the initial conditions of the models correspond to a simplified cross section of the Gulf of Corinth with a top-flattening part at the level of the tectonic window of Pheneos where the Phyllades nappe outcrops under the Tripolista nappe and the Pindos nappe (Figure 7).

[32] The two-dimensional assumption can be discussed because the dipping direction of the Phyllades nappe in the Gulf of Corinth is 30°/50°N while the stretching is directed along 00°N. This difference can produce either "en echelon" structures following the isodepth of the nappe, or reorient the fault in the dipping direction of the nappe. In fact, both of these structural patterns (en echelon faults and 30°N oriented faults) exist in the Gulf of Corinth.

7.1. Geological Settings

7.1.1. Rift Structural Pattern

[33] The azimuthal orientation of the rift is N120°, whereas the border faults are en echelon with azimuthal orientation at N90°/N100°. The uplift is clearly asymmetric between both shores of the Gulf and is emphasized by an abundance of synrift sediments uplifted up to 2 km on the southern shore, in contrast to their absence on the northern shore (see map in Figure 7). The southern shore exhibits four different basins (including the present one) which are related to major faults and spaced at 6 to 7 km distance from

one another. *Flotté* [2002] suggests that the ages of the basin decrease in a northward direction. Field observations also show that the first faults should have been rooted on the Phyllades nappe [*Flotté*, 2002]. Today, this contact zone is observed at about 1 km above sea level. Taking into account the maximum regional uplift of the Peloponnesus (2 mm yr^{-1}) and a reliable estimate for the age of the deformation (about 1 Myr), we can say that the fault rooted actually at only 1 or 2 km depth.

7.1.2. Evidence for Detachment/Decollement Level

[34] In the Central and Western part of the Gulf, the clusters of microseismicity are recorded between 5 and 12 km depth [*Rigo et al.*, 1996]. The structures outlined by these clusters have high-angle planar geometry (dipping about 70° to the north) and can be related to the faults on the southern shore. They root on a low 20°−30° north dipping plane [*Rigo et al.*, 1996; *Lyon Caen et al.*, 2002] seated below the northern shore.

7.1.3. Evidence of "Out-of-Sequence" Fault Activation

[35] In the frame of the northward migration of the southern shore of the rift, for the western part of the Gulf, we call "in sequence" a fault located northward of an older fault and "out-of-sequence" a fault that is found southward of the active faults. Present fault activity (Helike, Aigion, and offshore Aigion), structural observations [*Micarelli et al.*, 2003; *Ghisetti et al.*, 2001; *Moretti et al.*, 2003] as well as the geochemical data on fault cements [*Causse et al.*, 2004] show that several faults are active at the same time. Syn and postsedimentary out-of-sequence faults implying rollover in the sediments were detected in the footwall of the Helike fault [*Malartre et al.*, 2004].

7.1.4. Evidence That the Phyllades Nappe Constitutes a Preexisting Vertical Crustal-Scale Heterogeneity

[36] A dipping structure associated with concentrated microseismicity has been observed from seismic tomography [*Latorre et al.*, 2004] and corresponds to a localized variation of the Vs × VP and Vs/Vp velocities. These variations indicate the presence of lithological and fluid saturation contrasts. In addition, electrical magnetotelluric sounding highlights a positive conductivity anomaly [*Pham et al.*, 2000] above the dipping heterogeneity observed in the seismic tomography images. The authors of both articles suspect that these anomalies may be due to the presence of the Phyllades nappe at depth because it is mainly composed of phyllosilicates and the nappe constitutes the highest lithological contrast in the area.

7.2. Which Rifting Mode for Corinth?

[37] Our models suggest that the depth of the localization of the first synthetic fault is controlled only by the BDT in the weak nappe. This means that a realistic rheology to explain the first fault in Corinth should have its BDT as shallow as 2 km deep. On the other hand, seismicity is observed down to 10 km, implying that the competence contrasts between the nappe and the host rock must be high enough to permit rupture until this depth.

[38] After 30% of stretching, only the experiments 1a and 1b (Figures 8c and 8d) provide a satisfactory fit to the seismological data and the fault patterns (width of the faulted zone and number of major faults) in the Gulf of Corinth. Other models, which follow a typical rolling hinge pattern cannot reproduce at all the seismicity observed in the Gulf or the fault spacing. By comparing the last two models (1a and 1b) with the fault pattern and microseismicity, it appears that the best fit is obtained for the model with higher strain rate (1b) because in this case the major fault accumulates a larger displacement than in the case of model 1a. Moreover, 30% of stretching is obtained after 1.2 Myr in the case of model 1b and 1.8 Myr in the case of model 1a. As the age of the rift is supposed to be between 1.2 and 0.8 Myr [*Sorel*, 2000; *Moretti et al.*, 2003] the model with high background strain rate is the only one that can fit the width of the rift.
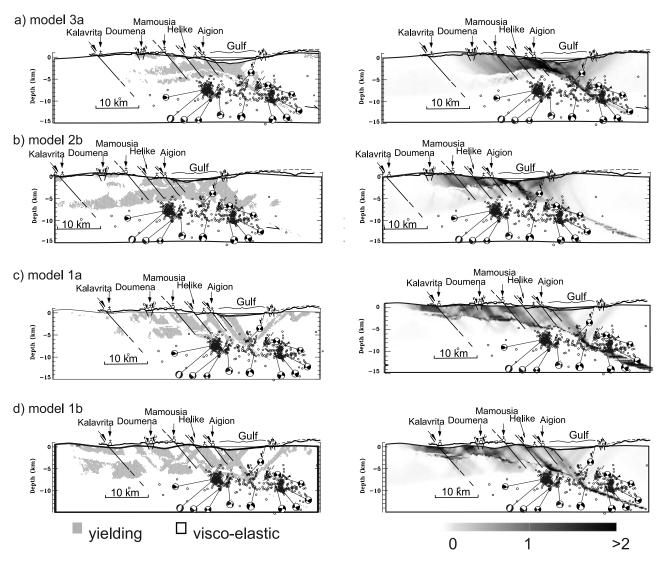
7.3. Implications for the Gulf of Corinth

7.3.1. Local Uplift of the Western Part of the Gulf of Corinth

[39] In the models, uplift of the southern basins occurs only after the depocenter migrates further north and when the topographic profiles reequilibrate isostatically. This can explain the acceleration of the uplift of the marine sediment with time highlighted by *De Martini et al.* [2002] in the area of Aigion as well as the subsidence profile proposed by *Ori* [1989]. This included a first phase of high subsidence rate (corresponding to the first deepening of the basin in the model until 10% stretching) followed by a low subsidence phase (corresponding to the fast migration of the depocenter and the reequilibration of the older basin at 15% and 25% in model 1b) and a recent increasing rate of subsidence phase (corresponding to the second basin formed between 25% and 30% in model 1b). In terms of time, our model predicts that subsidence rates slowed down 800 Myr ago, and that uplift of the southern coast begins between 400 Myr (20% of stretching) and 200 Myr (25% of stretching) ago. This timing is similar to the one suggested by *Moretti et al.* [2003] and V. Lykoussis et al. (Late Quaternary basin evolution of the gulf of Corinth: Sequence stratigraphy, sedimentation, fault slip and subsidence rates, submitted to *Marine Geology*, 2003) based on the analysis of the synrift sequences on subsurface data.

7.3.2. Regional Uplift

[40] The scale of our models is too small to account for possible regional uplift, due to, for instance, subduction of the Mediterranean lithosphere below the Peloponnesus. However, we have shown that heterogeneity due to the presence of a very weak nappe successfully explains the observed fault patterns. The resulting model actually fits the observed fault patterns and relative uplift/subsidence rate but does not reproduce the topography heights (only for the southern part of the Gulf). This suggests that these heights may be rather controlled by a regional uplift. This is confirmed by the fact that in the models, the nappe does not outcrop at the level of the first fault as is the case in the Gulf. This difference between models and field data suggests that the uplift rate in reality is larger than the rate obtained in our experiments. It confirms the idea that regional uplift rates must be in the order of 2 mm yr^{-1} in the southern coast of the western part of the Gulf [*Flotté*,
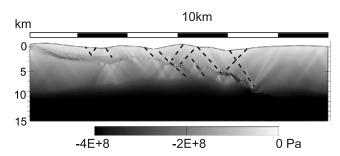
Figure 8. Fit to seismicity and fault pattern. The left column compares the occurrence of brittle strain in the model at 30% of stretching with *Rigo et al.* [1996] data on microseismicity. The right column shows the cumulative plastic strain and should be compared to fault patterns. Four cases are represented here. The first three cases (from top to bottom: 3a, 2a, 1a) correspond to increasing competence contrast to the bottom, and the last case (1b) to a higher stretching rate (1.5 cm yr^{-1} instead of 1 cm yr^{-1}). The first model is not acceptable because the fault zone is not wide enough to be representative of the Gulf of Corinth; the fault pattern does not show any kind of major faults, and microseismicity is localized in the weakest and ductile part of the model. The second case fits better with microseismicity, but the fault zone is not representative of the Gulf of Corinth. The last two are acceptable in terms of faulting patterns (width and number of major faults). The one with a higher strain rate is preferred because in this model, the fault, corresponding to the Helike fault, has accumulated a large amount of displacement, while in the lower strain rate model, the same fault accumulates only minor displacement.

2002], thus significantly higher than the regional uplift calculated by *Armijo et al.* [1996] (less than 0.5 mm yr^{-1}) at the level of Xylocastro.

7.3.3. Regional Geodynamics

[41] The GPS data in the Gulf of Corinth [*Briole et al.*, 2000] indicates that present opening rates are much faster in the western part (1.5 cm yr^{-1}) than in the eastern part (0.5 cm yr^{-1}). These measurements are not compatible with the GPS displacement and finite strain measurements obtained for the Aegean domain (see, e.g., *Jolivet* [2001] for comparison), which imply a faster opening rate in the east than in the west [*Jolivet*, 2001; *Jolivet et al.*, 1994]. Our results show that in the western part, a constant high strain rate (1.5 cm yr^{-1}) explains better the geometry of the faults than an average strain rate (1 cm yr^{-1}). It validates the hypothesis that the GPS-based rates of extension could be

Figure 9. Pressure field around the nappe. This picture represents the pressure field for model 1b after 30% of stretching; the faults (dashed lines) are associated with underpressure; the nappe (darker gray) is associated with overpressure. The nappe thus forms a pressure barrier against upward flow under the forming basin.

extrapolated to the whole extension history of the Gulf, and one may note that this constant slip rate leads to a nonconstant subsidence rate and kinematics of faults due to the heterogeneity of the material. The westward growing opening rate must thus be explained either by dynamic processes (e.g., the difference in crustal thickness between both the eastern and western parts of the Gulf), or by kinematics constraints independent of the Aegean Sea extension (e.g., the propagation of the North Anatolian fault and the inversion of strike on the Kefalonia fault [*Cocard et al.*, 1999]). Our model is not valid to discriminate between these two hypotheses, i.e., local versus regional acceleration, however, *Le Pourhiet et al* [2003] have shown that the existence of thickened crust below the Corinth rift is nonnegligible and can lead to a local increase of extension rate in the western part of the Gulf.

7.3.4. Fluid Circulation

[42] Our numerical code operates with full stresses and thus has the advantage of handling pressure in a self-consistent way. This allows us to obtain spatial pressure distributions that can be matched with the deformation history instead of assuming that pressure is only depth dependent. Figure 9 shows pressure predicted by our best fitting model (1b) for present state. In Figure 9, the faults exhibit underpressure, while the nappe exhibits high overpressure. Assuming that in a porous medium fluids flow in the direction of an inverse pressure gradient (which was first shown by Pythagoras (450BC) and is well confirmed for geothermal systems), Figure 9 suggests that fluids can be driven along faults in the southern part of the rift. Yet, under the recent subsiding part of the rift, where the microseismicity localizes, the nappe should constitute a pressure barrier to upward flow. The resulting flow patterns correlate with the location of electric sounding and seismic tomography anomalies described in the previous sections.

7.4. Conclusions for the Western Gulf of Corinth

[43] Only the experiments based on the assumption of high competence contrast fit the fault pattern and microseismicity of the Gulf of Corinth. Regional uplift is thus needed to explain that the contact between the Gulf's southern fault and Phyllades nappe is outcropping. The best fit between the model and observations is obtained in experiment 1b (high

competence contrast and high (1.5 cm yr^{-1}) background strain rate). In this model, the uplift of the southern coast is late and starts after the beginning of the migration of the rift's depocenter. This model also explains the existence of out-of-sequence faults dipping in the direction of the recent basin (out-of-sequence type II fault). It may also explain the electric conductivity anomalies and seismic velocity anomalies observed from magnetotelluric and tomographic sounding data because the presence of the nappe may create a pressure barrier for fluid ascent below the present Gulf.

Appendix A: Numerical Implementation

[44] In the following, stress σ and strain rate $\dot{\varepsilon}$ tensors are separated into their deviatoric and isotropic parts:

$$\begin{aligned} \overline{e} &= \dot{\varepsilon}_{ii}/3 \\ e_{ij} &= \dot{\varepsilon}_{ij} - \delta_{ij}\overline{e} \\ \overline{\sigma} &= \sigma_{ii}/3 \\ \tau_{ij} &= \sigma_{ij} - \delta_{ij}\overline{\sigma}. \end{aligned} \tag{A1}$$

This allows us to define viscoelastic rheology using two parameters G (shear modulus) and μ (shear viscosity) in shear.

$$\left.\begin{aligned} e^{\text{elas}} + e^{\text{vis}} - e &= 0 \\ e^{\text{elas}} &= \dot{\tau}/2G \\ e^{\text{vis}} &= \tau/2\mu \\ \dot{\tau}_{ij} &= 2G\left(e_{ij} - \tau_{ij}\Big/2\mu\left(T,e^{\text{II}},\tau_{ij},\overline{\sigma}\right)\right) \end{aligned}\right\}, \tag{A2}$$

where T is the temperature, e is total shear strain rate, and superscript "II" stands for the second invariant.

[45] Following common assumptions, bulk viscosity is neglected in para(o)voz; the isotropic stress update rule is thus written only as a function of elastic bulk modulus K

$$\dot{\overline{\sigma}} = 3K\overline{e}. \tag{A3}$$

[46] Mohr-Coulomb elastoplastic behavior is chosen instead of viscoelastic rheology if the shear failure criteria F reaches zero and the associated effective shear stress is smaller than that for viscous flow

$$\left.\begin{aligned} \text{F} &= \tau^* + \sin\Phi\sigma^* - \cos\Phi Co \\ \tau^* &= \sqrt{(\tau_{11} - \tau_{22})^2/4 + \tau_{12}^2} \\ \sigma^* &= (\sigma_{11} + \sigma_{22})/2 = (\tau_{11} + \tau_{22})/2 + \overline{\sigma} \end{aligned}\right\}, \tag{A4}$$

where Φ is the angle of internal friction. In fact, we also test for tension failure criteria, which, however, is not dominant in the conditions of our experiments, and its description is thus omitted due to lack of space.

[47] The plastic flow law $\dot{\varepsilon}^{plas}$ is deduced using plastic potential function Q and a scalar plastic multiplier λ

$$\left.\begin{array}{l} Q = \tau^* + \sin\Psi\sigma^* \\[1em] \dot{\varepsilon}_{ij}^{plas} = \lambda\dfrac{\partial Q}{\partial\sigma_{ij}} \end{array}\right\}, \qquad (A5)$$

where Ψ stands for dilatancy angle, $\Psi = \Phi - 30° \approx 0°$ for most rocks.

[48] The as yet unknown value of scalar λ is found from the consistency criteria:

$$\frac{F(\lambda) - F^{old}}{dt} = 0. \qquad (A6)$$

[49] Finally, using the above equations the stress update rule becomes

$$\left.\begin{array}{l} \dot{\tau}_{ij} = 2G\left(e_{ij} - \lambda\partial Q/\partial\tau_{ij}\right) \\[0.8em] \partial Q/\partial\overline{\sigma} = \sin\Psi \\[0.8em] \dot{\overline{\sigma}} = 3K\left(\overline{e} - \lambda\sin\Psi/3\right) \end{array}\right\}. \qquad (A7)$$

Once the new velocity field has been calculated using Newtown's Second Law (equation (1)), stress is updated to take into account objectivity to rotation of the stress tensor by using Jauman's corotational stress time derivative:

$$\left.\begin{array}{l} \overset{\vee}{\sigma}_{ij} = \sigma_{ij} + \left(\omega_{ik}\sigma_{kj} - \sigma_{ik}\omega_{kj}\right)\Delta t \\[1em] \omega_{ij} = \dfrac{1}{2}\left\{\dfrac{\partial V_i}{\partial x_j} - \dfrac{\partial V_j}{\partial x_i}\right\} \end{array}\right. . \qquad (A8)$$

References

Armijo, R., B. Meyer, G. C. P. King, A. Rigo, and D. Papanastassiou (1996), Quaternary evolution of the Corinth rift and its implications for the late Cenozoic evolution of the Aegean, *Geophys. J. Int.*, *126*, 11–53.

Axen, G. J. (1992), Pore pressure, stress increase, and fault weakening in low-angle normal faulting, *J. Geophys. Res.*, *97*, 8979–8991.

Axen, G. J., and J. M. Bartley (1997), Field tests of rolling hinges: Existence, mechanical types, and implications for extensional tectonics, *J. Geophys. Res.*, *109*, 20,515–20,537.

Bertotti, G., and Y. Y. Podladchikov (2000), Dynamic link between the level of ductile crustal flow and style of normal faulting of the brittle crust, *Tectonophysics*, *320*, 195–218.

Brace, W. F., and D. L. Kohlstedt (1980), Limits on lithospheric stress imposed by laboratory experiments, *J. Geophys. Res.*, *85*, 6248–6252.

Briole, P., A. Rigo, H. Lyon Caen, J. Ruegg, K. Papazissi, C. Mistakaki, A. Balodimou, G. Veis, D. Hatzfeld, and A. Deschamps (2000), Active deformation of the Corinth rift, Greece: Results from repeated Global Positioning System surveys between 1990 and 1995, *J. Geophys. Res.*, *105*, 25,605–25,625.

Buck, W. R. (1991), Modes of continental lithospheric extension, *J. Geophys. Res.*, *96*, 20,161–20,178.

Burov, E. B., and M. Diament (1995), The effective elastic thickness (T_e) of continental lithosphere: What does it really mean?, *J. Geophys. Res.*, *100*, 3905–3927.

Burov, E. B., and A. N. B. Poliakov (2001), Erosion and rheology controls on synrift and postrift evolution: Verifying old and new ideas using a fully coupled numerical model, *J. Geophys. Res.*, *106*, 16,461–16,481.

Causse, C., I. Moretti, R. Eschard, L. Micarelli, B. Ghaleb, and N. Frank (2004), Kinematics of the Corinth Gulf inferred from calcite dating and syntectonic sedimentary characteristics, *C. R. Geosci.*, *336*, 281–290.

Cocard, M., H. Khale, Y. Peter, A. Geiger, G. Veis, S. Felekis, D. Paradissis, and H. Billiris (1999), New constraints on the rapid motion of the Aegean region: Recent results inferred from GPS measurements (1993) across the West Hellenic Arc, Greece, *Earth Planet. Sci. Lett.*, *172*, 39–47.

Culling, W. E. H. (1960), Analytical theory of erosion, *J. Geol.*, *68*, 333–336.

Cundall, P. A. (1989), Numerical experiments on localization in frictional materials, *Ing. Arch.*, *59*, 148–159.

De Martini, P. M., D. Pantosti, N. Palyvos, F. Lemeille, L. McNeil, and R. Collier (2002), Slip rates of the Aigion and Eliki faults from uplifted marine terraces, Corinth Gulf Greece, *Geophys. Res. Abstr.* [CD-ROM], *4*, EGS02-A-05710.

Flotté, N. (2002), Caractérisation structurale et cinématique d'un rift sur détachement: Le rift de Corinthe-Patras, Grèce, Ph.D. thesis, 197 pp., Univ. Paris Sud, Orsay, France.

Ghisetti, F. C., L. Vezzani, F. Agosta, R. Sibson, and I. Moretti (2001), Tectonic setting and sedimentary evolution of the south-west margin of the Corinth rift (Aigion-Xylocastro area), Inst. Fr. du Pet., Rueil Malmaison, France.

Hansen, F. D., and N. L. Carter (1982), Creep of selected crustal rocks at 1000 MPa, *Eos Trans. AGU*, *63*, 437.

Heiskanen, W. A., and F. A. V. Meinesz (1958), *The Earth and Its Gravity Field*, 470 pp., McGraw-Hill, New York.

Jacobshagen, V., S. Duerr, F. Kockel, K. Kopp, and G. Kowalczyk (1978), Structure and geodynamic evolution of the Aegean region, in *Alps Apennines, Hellenides: Geodynamic Investigation Along Geotraverses by an International Group of Geoscientists, Inter-Union Comm. Geodyn. Sci. Rep.*, vol. 38, edited by H. Closs et al., pp. 537–620, Schweizerbart, Stuttgart, Germany.

Jolivet, L. (2001), A comparison of geodetic and finite strain pattern in the Aegean, geodynamic implications, *Earth Planet. Sci. Lett.*, *187*, 95–104.

Jolivet, L., J. P. Brun, P. Gautier, S. Lallemant, and M. Patriat (1994), 3D kinematics of extension in the Aegean region from the early Miocene to the present, insights from the ductile crust, *Bull. Soc. Geol. Fr.*, *165*, 195–209.

Kaufman, P. S., and L. H. Royden (1994), Lower crustal flow in an extensional setting: Constraints from the Halloran Hills region, eastern Mojave Desert, California, *J. Geophys. Res.*, *99*, 15,723–15,739.

Kirby, S. H., and A. K. Kronenberg (1987), Rheology of the lithosphere: Selected topics, *Rev. Geophys.*, *25*, 1219–1244.

Latorre, D., J. Virieux, T. Monfret, and H. Lyon-Caen (2004), Converted seismic wave investigation in the Gulf of Corinth Gulf from local earthquakes, *C. R. Geosci.*, *336*, 259–267.

Le Pourhiet, L., E. Burov, and I. Moretti (2003), Initial crustal thickness geometry controls on the extension in a back arc domain: Case of the Gulf of Corinth, *Tectonics*, *22*(4), 1032, doi:10.1029/2002TC001433.

Lyon Caen, H., K. Makopoulos, P. Papadimitriou, A. Deschamps, P. Bernard, F. Pachianni, S. Bourouis, H. Castarede, and F. Cornet (2002), Seismicity in the Aigion area as seen by the Corinth Rift seismological network, *Geophys. Res. Abstr.* [CD-ROM], *4*, EGS02-A-05400.

Malartre, F., M. Ford, and E. A. Williams (2004), Preliminary biostratigraphy and 3D geometry of the Vouraikos Gilbert-type fan delta, Gulf of Corinth, Greece, *C. R. Geosci.*, *336*, 269–280.

Melosh, H. J. (1990), The mechanics of low angle normal faulting in the Basin and Range, *Nature*, *343*, 331–335.

Micarelli, L., I. Moretti, and J. M. Daniel (2003), Influence of depth and amount of displacement of the characteristics of normal faults, case study in the Gulf of Corinth-Greece, *J. Geodyn.*, *36*, 275–303.

Montési, L. G. J., and M. T. Zuber (2003), Spacing of faults at the scale of the lithosphere and localization instability: 1. Theory, *J. Geophys. Res.*, *108*(B2), 2110, doi:10.1029/2002JB001923.

Moretti, I., D. Sakellariou, V. Lykousis, and L. Micarelli (2003), The Gulf of Corinth: A half graben?, *J. Geodyn.*, *36*, 323–340.

Ori, G. G. (1989), Geological history of the extensional basin of the gulf of Corinth (Miocene Pleistocene), Greece, *Geology*, *17*, 918–921.

Parsons, B., and J. G. Sclater (1977), An analysis of the variation of ocean floor bathymetry and heat flow with age, *J. Geophys. Res.*, *82*, 803–827.

Pham, V. N., P. Bernard, D. Boyer, G. Chouliaras, J. L. L. Mouël, and G. N. Stavrakakis (2000), Electrical conductivity and crustal structure beneath the central Hellenides around the Gulf of Corinth (Greece) and their relationship with the seismotectonics, *Geophys. J. Int.*, *142*, 948–969.

Poliakov, A. N. B., and W. R. Buck (1996), Faulting due to stretching of viscoelastic-plastic lithosphere;

some remarks on brittle-ductile transition, rift shoulders and depth of necking, *Eos Trans. AGU*, *77*(46), Fall Meet. Suppl., F702.

Poliakov, A. N. B., Y. Y. Podladchikov, and C. Talbot (1993), Initiation of salt diapirs with frictional overburden: Numerical experiments, *Tectonophysics*, *228*, 199–210.

Ranalli, G. (1987), *Rheology of the Earth: Deformation and Flow Processes in Geophysics and Geodynamics*, 366 pp., Allen and Unwin, Boston, Mass.

Rigo, A., H. Lyon-Caen, R. Armijo, A. Deschamps, D. Hatzfeld, K. Makropoulos, P. Papadimitriou, and I. Kassaras (1996), A microseismic study in the western part of the Gulf of Corinth (Greece): Implications for large-scale normal faulting mechanisms, *Geophys J. Int.*, *126*, 663–688.

Sorel, D. (2000), A Pleistocene and still active detachment fault and the origin of Corinth Patras rift, Greece, *Geology*, *28*, 83–86.

Spadini, G., and Y. Y. Podladchikov (1996), Spacing of consecutive normal faulting in the lithosphere: A dynamic model for axis jumping (Tyrrhenian Sea), *Earth Planet. Sci. Lett.*, *144*, 21–34.

Tsenn, M., and N. Carter (1987), Upper limits of power law creep of rocks, *Tectonophysics*, *136*, 1–26.

Westaway, R. (2002), The Quaternary evolution of the Gulf of Corinth, central Greece: Coupling between surface processes and flow in the lower crust, *Tectonophysics*, *348*, 269–318.

————————

E. Burov and L. Le Pourhiet, Laboratoire de Tectonique, UMR 7072, Université Pierre et Marie Curie, 4 place Jussieu, F-75252 Paris Cedex 05, France. (laetitia.lepourhiet@lgs.jussieu.fr)

I. Moretti, Institut Français du Pétrole, 1-4, avenue de Bois Préau, F-92852 Rueil Malmaison, France.

Figure 2. Second invariant of stress and cumulative plastic strain. For all models presented here, the viscoelastoplastic rheological parameters of the host rocks (phase 4, Table 1) and of the background strain rates are identical, only the competence contrasts vary. Effective shear stress is shown here for high, intermediate, and low competence contrasts at different stages of stretching (5, 10, 20, and 30%). The purple color corresponds to the highest deviatoric stress. The bottom pictures in each column represent cumulated plastic (brittle) strain. The blue regions are those which always deform viscously. The red color represents zones where accumulated brittle strain is very high (these parts are interpreted as major faults). At each step, the currently active faults, on which the current strain rates are highest, are marked with dashed lines. At 5% stretching, all models have their integrated strength (deviatoric stress integrated on a vertical profile in the faulted zone) reduced at the level where faulting takes place. The model with the highest integrated strength is the model with low competence contrast. The model with very high competence contrast has almost negligible strength. (a) High competence contrast (model 1a). Between 10 and 20% stretching, basin migrates, strain is distributed, because (1) the nappe is so weak that it is always easier to break somewhere else and (2) the decollement level is very shallow and many faults are needed to accommodate strain. At 30% stretching, many synthetic faults are active, the subsiding basin is 13 km wide, and the stress patterns do not indicate any localized weakening of the crust. Plastic strain indicates that four major faults were formed during the deformation. (b) Intermediate competence contrast (model 2a). In this case, the basin does not migrate as much as in the case of the high competence contrast, but the number of the active faults increases with time as the width of the basin increases. The nappe behaves as a level of decollement where the faults are refracted, which causes faulting to be shifted between surface and depth. At 30% stretching, the crust is weakened locally by an upward flow of hot lower crust induced by an isostatic response to surface unloading. The thinning of the crust is symmetric even if synthetic faults are predominant. Plastic strain indicates that two major faults were formed during the deformation. (c) Low competence contrast (model 3a). From 5 to 30% stretching, the width of the subsiding basin decreases from 30 km to 15 km. The depocenter migrates smoothly in the dipping direction of the nappe by a rolling hinge mechanism until 20% stretching. At that point, the crust is weakened locally by hot lower crust material. The migration is fast because none of the faults accumulate important strain, apart from the last one where strain finally localizes.
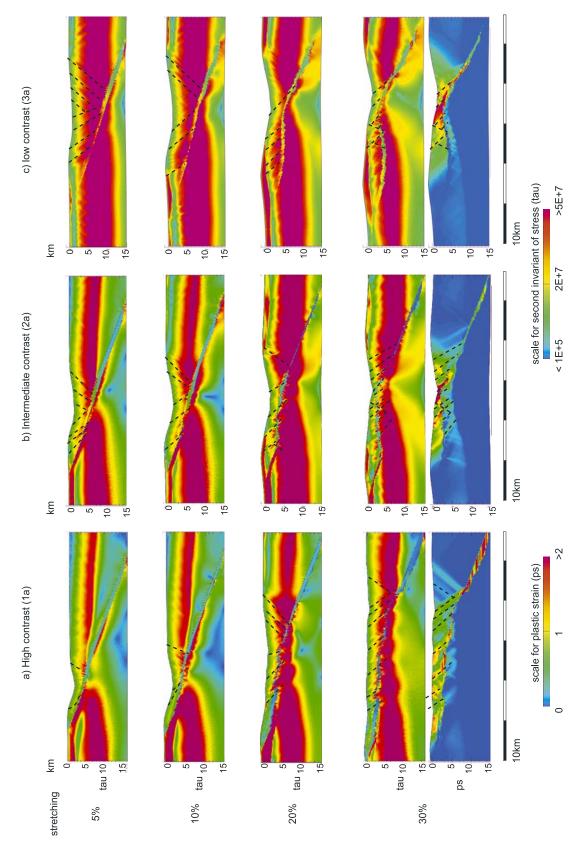
Figure 2